PAPER

# Remanence enhancement for stray field-based applications in arrays of crystalline nanomagnets

IOP Publishing Journal of Physics D: Applied Physics
J. Phys. D: Appl. Phys. **52** (2019) 095002 (11pp) https://doi.org/10.1088/1361-6463/aaf614

# Remanence enhancement for stray field-based applications in arrays of crystalline nanomagnets

**F Cebollada[1,5], A Gomez[2,6], F J Palomares[3], M Sanchez-Agudo[1], E M Gonzalez[2,4], U Urdiroz[1,3], J L Vicent[2,4] and J M Gonzalez[3]**

[1] POEMMA-CEMDATIC, Universidad Politécnica de Madrid, 28040 Madrid, Spain
[2] Facultad CC. Físicas, Departamento Física de Materiales, Universidad Complutense, 28040 Madrid, Spain
[3] Instituto de Ciencia de Materiales de Madrid (CSIC), Sor Juana Inés de la Cruz, 3, 28049 Madrid, Spain
[4] IMDEA-Nanociencia, Cantoblanco, 28049 Madrid, Spain

E-mail: fcebollada@etsit.upm.es

Received 31 August 2018, revised 21 November 2018
Accepted for publication 4 December 2018
Published 28 December 2018

**Abstract**

With the aim of achieving stable, substantial remanences adequate for exploitation in stray field-based applications, we report on the hysteresis behavior occurring in arrays of single-crystal Fe motifs, e-beam lithographed into prisms with triangular bases and different orientations of their magnetocrystalline axes with respect to the morphological symmetry axes. From both experimental and simulational analyses we recognize the fact that the magnetization reversal processes of our samples were mediated by motif-sized vortices. Their nucleation and annihilation fields and sites within the motifs, and their field-induced displacements, are discussed in terms of the magnetocrystalline and configurational anisotropies and inter-motif dipolar interactions. From our data, we conclude that reduced remanences as large as 0.85 (sufficient for the application requirements), protected by nucleation fields of several tens of Oe, can be produced in arrays where magnetocrystalline easy axes reinforce and partly compensate the easiest and hardest configurational ones, respectively. The angular dependence of the reduced remanence associated with interplay of these anisotropies corresponds to a symmetry reduction from the triaxial one linked to the triangular morphology down to an effective uniaxial one. We also identify, for the particular case of inter-nanoprism distances that are short in comparison with the dimensions of the motif base, a contribution to the remanence enhancement originating from the dipolar interactions.

Keywords: nanomagnets, remanence enhancement, configurational anisotropy, magnetocrystalline anisotropy, dipolar interactions

(Some figures may appear in colour only in the online journal)

## Introduction

Nanomagnet arrays have a sizeable potential for use in technological applications in fields such as spintronics, magnetic storage, sensors and high-frequency electronic components [1–5]. To a large extent, that potential is related to the considerable degree of hysteretic control achievable through easily modifiable array parameters such as motif morphology and motif lattice symmetry and periodicity. The main requirement for utilizing the specific, optimized extrinsic magnetic properties of these arrays is understanding the role played by the different energy contributions governing their magnetization reversal mechanisms [6]. In particular, arrays of triangular

[5] Author to whom any correspondence should be addressed.
[6] Present address: Centro de Astrobiologia (CSIC-INTA), Torrejon de Ardoz, 28850 Madrid, Spain.

magnetic dots have recently been proposed for use in magnetically switchable devices based on hybrid superconductor/ferromagnetic bilayers, which use the ratchet effect to rectify the ac-driven movement of superconductor vortices [7]. Magnetic nanomotifs with triangular morphology have also been employed in combined memory/logic gates devices in which the input bits are defined through the magnetization state at two nanotriangle vertices while the output one corresponds to the magnetization orientation at the third vertex [8, 9]. These applications operate on the basis of the stray fields created by the nanomagnets in their remanent state, and thus require remanences that are as large and stable as possible.

In magnetic nanomotifs, the angular dependence of the energy of the extended, inhomogeneous magnetic moment configurations that mediate the motifs' magnetization reversal, generally known as configurational anisotropy [10–12], frequently dominates the reversal process (and that of arrays of weakly interacting motifs). The configurational anisotropy is a motif-scale contribution of the magnetostatic energy (MSE) to the total array energy, which depends on the geometry of the nanomagnets (motif shape and size) and their magnetic properties (spontaneous magnetization, magneto-crystalline and/or other anisotropy and exchange constant). One of the most ubiquitous inhomogeneous magnetic moment structures is the vortex configuration. This is a solenoidal moment structure characterized by reduced global magnetization which is very effective in reducing the MSE of the motifs: in the particular case of a nanodot, the occurrence of an undistorted, centered vortex corresponds to local moments parallel to the lateral surfaces of the motif (an absence of magnetic poles at those surfaces and of stray fields outside the dot) and configurational isotropy [12–18]. Vortices occurring in the motif size range intermediate between those corresponding to single and multidomain regimes nucleate when the applied field decreases from saturating values down to the so-called nucleation field $H_n$. Once a vortex is nucleated, and for increasing applied demagnetizing fields (or, if nucleation occurs in the first quadrant, decreasing magnetizing fields), its central core moves across the motif, tending to become marginally stable under close-to-zero applied fields at a position usually located near the center of the motif. Importantly, this is a close-to-zero remanent magnetization state that is not adequate for the implementation of stray field-based applications. Finally, for increasing demagnetizing fields, the vortex exits for nanodots at the annihilation field $H_{an}$, making possible an approach to negative saturation. The formation of the vortices requires the easy orientation of most of the motif moments along a broad range of in-plane directions. This has stimulated the analysis of the dynamics of the vortices in close-to-zero anisotropy phases, as exemplified by Permalloy [10–19]. Different strategies have been employed to gain control of the critical fields and displacements of the vortices and, through these parameters, of global motif reversal. The feasible approaches to enhancing the remanence are based on the consideration of reduced symmetry shapes such as those present in rods, ellipses, triangles and edge-cut circular dots, in combination with the use of different orientations of the magnetizing field [20–25]. The effect on the nucleation and annihilation fields of the motif geometry is usually convoluted with the array lattice symmetries and dimensions (e.g. inter-dot distances [25–27]).

In this paper, and with the aim of obtaining significant remanences suitable for the exploitation of nanomagnet arrays in stray field-based applications, we present an experimental and micromagnetic simulational study of the interplay among the configurational and magnetocrystalline anisotropies and inter-motif dipolar interactions taking place in square arrays of nanomagnets patterned from single-crystal Fe films for different orientations between their morphological symmetry and magnetocrystalline easy axes.

## Experimental and simulational techniques

Arrays of Fe nanomotifs were fabricated on epitaxial Au(0 0 1)/Fe(0 0 1)/MgO(0 0 1) films grown by a combination of molecular beam epitaxy and pulsed laser deposition. The thickness of the Fe films and of the Au capping layer was 25 nm and 10 nm, respectively. A detailed study of the structure and crystallinity of the precursor films was carried out using x-ray diffraction (including asymmetric phi-scans) and reflectivity, with both conventional and synchrotron radiation sources; this confirmed their single-crystal nature [6, 28]. This point was confirmed from the results of the measurement of the in-plane angular dependence of the ferromagnetic resonance which evidenced a very well defined biaxial symmetry.

Each engraved pattern consisted of a lattice of nanoprisms with triangular bases (in the following these motifs will be named NTs, whereas the triangles at their bases will be named NTBs). The NTs were fabricated by electron beam lithography following a procedure described in a previous paper [6]. The reference axes we considered corresponded to an in-plane *X* axis oriented parallel to the NTB bases and an in-plane *Y* axis parallel to the NTB heights (see figure 1). The unit cell dimensions (see table 1) of array A1 (A2) were 775 (760) nm along the *X* axis and 750 (770) nm along the *Y* axis. In order to take into consideration weaker inter-motif interactions than those occurring in arrays A1 and A2, a second set of arrays (NI-A1 and NI-A2) was implemented with a distance between neighboring motifs in array NI-A1 (NI-A2) of 1400 nm (1400 nm) along both the *X* and *Y* axes. Also, and with the aim of more clearly identifying the consequences of the configurational anisotropy of the nanomagnets, they were designed in arrays A1 and A2 with an isosceles shape, and consequently with a slight symmetry reduction with respect to the equilateral triangular morphology. Namely, the NTs had lateral edges that were slightly shorter than that of their bases, and their dimensions were base 620 (585) nm and height 480 (475) nm for arrays A1 (A2). In this respect, we recall the fact that the configurational easy axis distribution occurring in our (isolated) isosceles NTs corresponds to an easiest axis parallel to the NTB bases (*X* axis) and two less easy axes, having larger energies than the *X* axis and being directed parallel to the two NTB sides having equal length.

The maximum energy (hardest) configurational axis coincides with the *Y* axis, and there are two hard axes having a lower energy than the *Y* axis, oriented along the perpendiculars

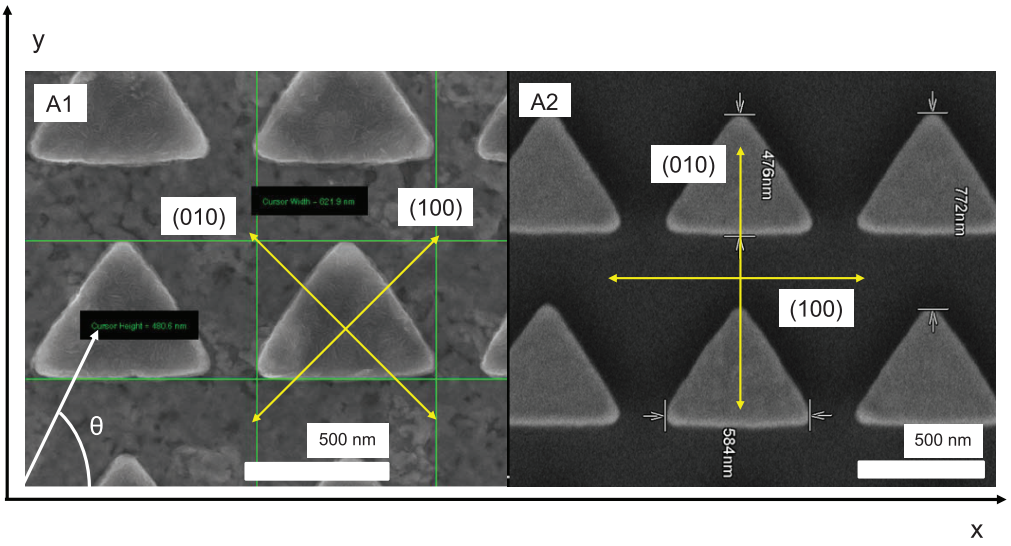


**Figure 1.** Scanning electron microscope image of arrays A1 and A2 showing the orientation of the magnetocrystalline axes (see text). The coordinate $X$ and $Y$ axes and the angle $\theta$ used throughout the paper are also shown [7].

**Table 1.** Array identifications and their corresponding motif dimensions, motif lattice parameters along the $X$ and $Y$ axes (parallel and perpendicular to the NT bases, respectively) and magnetic anisotropy easy axis configuration (see text). MAE is magnetocrystalline anisotropy energy.

| Array name | Motif base (nm) | Motif height (nm) | Unit cell dimension $X$ axis (nm) | Unit cell dimension $Y$ axis (nm) | MAE easy axes |
|---|---|---|---|---|---|
| A1 | 620 | 480 | 775 | 750 | x |
| A2 | 585 | 475 | 760 | 770 | + |
| NI-A1 | 600 | 520 | 1400 | 1400 | x |
| NI-A2 | 600 | 520 | 1400 | 1400 | + |

to the two NTB sides of equal length [29, 30]. In the case of the reduced interaction arrays (NI-A1 and NI-A2), the engraved NTs had equilateral NTBs and the same dimensions in both arrays, namely 600 nm (base) and 520 nm (height). The (in-plane) easy magnetocrystalline anisotropy energy (MAE) axes of the NTs corresponded to the [1 0 0] and [0 1 0] crystallographic directions, and were oriented in arrays A1 and NI-A1 by forming an angle of $\pi/4$ with the $X$ and $Y$ axes, respectively (the '$\times$' configuration), whereas in the case of arrays A2 and NI-A2 the MAE easy axes were directed parallel to the reference system $X$ and $Y$ axes, respectively (the '+' configuration).

The hysteretic behavior of the arrays was studied at room temperature (RT) by means of a magneto-optic Kerr effect (MOKE) set-up. The magnetization configurations associated with applying the field along different (in-plane) directions were analyzed from the results of micromagnetic simulations carried out using OOMMF [31] (a code that does not incorporate any thermal effects and which therefore provides information corresponding to 0 K). Sets of four NTs with sizes and separations consistent with the experimental ones and material parameter values corresponding to RT Fe [32] (saturation magnetization $M_S$ $1.7 \times 10^6$ A m$^{-1}$, exchange constant $A = 2.1 \times 10^{-11}$ J m$^{-1}$ and second order anisotropy constant $K = 4.8 \times 10^4$ J $\cdot$ m$^{-3}$) were simulated.

## Results and discussion

The hysteresis loops measured in array A1 (the '$\times$' configuration) by applying a field parallel to the $X$ and $Y$ axes are plotted in figures 2(a) and (b), respectively (solid symbols joined by lines). The insets in figures 2(a) and (b) show the field dependences of the differential susceptibilities measured along each loop demagnetization branch. For both applied field directions the differential susceptibility shows two maxima in the second quadrant and, between them, a shallow minimum that in the loops is associated with some degree of constriction. The measured loops exhibit modest to low remanence-to-saturation, $m_r$, values: 0.6 for the field applied along the $X$ axis and 0.3 for the field applied along the $Y$ axis. The micromagnetic data corresponding to these loops (continuous lines in figures 2(a) and (b)) show that the simulations retain the main features of the experimental results. The loop calculated with the field parallel to the $X$ axis, plotted in figure 2(a), is rather square and presents two high-susceptibility demagnetization stages (occurring in the second quadrant) followed by evolution of a lower-susceptibility magnetization towards the negative saturation occurring in a field range coincident with that associated with the experimental highest field maximum differential susceptibility. The calculated remanence and coercivity are slightly above the experimental ones; this can be linked

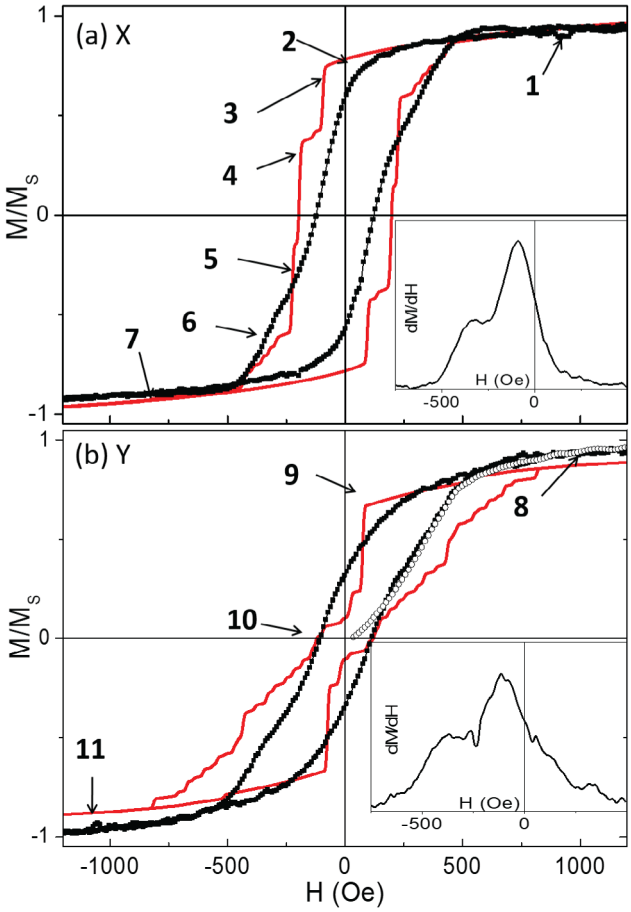


**Figure 2.** Array A1: experimental (symbols joined by lines) and calculated (continuous lines) hysteresis loops corresponding to applied fields directed along the *X* axis (a) and *Y* axis (b). The labels in these figures correspond to those tagging the moment configurations obtained from the micromagnetic simulations shown in figure 3. The magnetization curves measured by applying the field along (a) the *X* axis and (b) the *Y* axis, with the array in a remanent state prepared after saturation with the field applied along *Y* and *X* axes, respectively, are plotted with open circles. Insets: field dependence of the differential susceptibility along the demagnetization branches of the experimental loops.

to the absence of defects in the model (either morphological or related to the local magnetic properties) that could favor vortex nucleation within the NT. Examination of the magnetic moment configurations mediating the A1 array motif demagnetization process allows us to identify the fact that the global reversal progresses from the initial departures from saturation, through the nucleation of a vortex-type moment structure, vortex displacement and marginal stabilization near the NTB center, vortex annihilation and the approach to reversed saturation. The associated moment configurations (being independent of NT thickness discretization) are summarized in figure 3, in which the labels of the configurations correspond to the labels in the loops in figure 2 and the arrows below the NTs indicate the applied field direction and approximate magnitude (no relevant differences between the magnetic moment configurations obtained in the four motifs simulating the array were found in any of the cases considered). For array A1 and a field applied parallel to the *X* axis the vortex is nucleated at the NTB base (label 3 in figure 3), moves to the NTB center (labels 4 and 5 in figure 3) and leaves the motif through the upper NTB vertex (label 6 in figure 3). The remanent configuration (label 2 in figure 3) corresponds to the fanning of most of the motif moments from and towards the vertices at the extremes of horizontal side of the NTB, thus globally resembling a 'C' shape. This is the known *buckle configuration* [30, 33].

For a field applied parallel to the *Y* axis the vortex is nucleated from a 'Y' configuration [30, 33], a moment structure symmetrical with respect to a line joining the base midpoint and the NTB apex and corresponding to a fanning of the moments from the vertices at the base of the NTB towards its apex, thus resembling an inverted 'Y' (label 8 in figure 3). Nucleation occurs at one of the sides of the NTB (label 9 in figure 3), after which the vortex moves to the motif center (label 10 in figure 3; remanence configuration) and it leaves the NT through the NTB vertex on the side opposite that at which the nucleation occurred (label 11 in figure 3). In *Y* axis field loops in array A1, the calculated and experimental coercivities almost coincide but the total susceptibility obtained from the simulation is clearly lower than the experimental one, as can be seen in figure 2(b). We understand this result as a consequence of the fact that the vortex can be easily stabilized in the array A1 motifs near the NTB center. The high vortex stability in that region is due to the characteristics of the configurational and MAE contributions to the motif energy: the easy MAE axes are close to parallel to the intermediate-energy hard configurational axes. This renders the NT more isotropic than a motif having an exclusive configurational anisotropy and it allows the stable adaptation of the moment configurations to the global triangular morphology. As a consequence, in the absence of defects (as in the case of the simulated nanomagnets), higher fields are required to annihilate the vortices and saturate the motifs.

The hysteresis loops measured in array A2 by applying the field parallel to the *X* and *Y* axes are plotted in figures 4(a) and (b), respectively (solid symbols joined by lines). Both loops evidence a global reversal process taking place through two irreversible stages with high differential susceptibility. Also, both loops show the occurrence of a well-defined loop constriction in the magnetization field range close to zero. The loop measured by applying the field parallel to the *X* axis exhibits higher reduced remanence ($m_r = 0.85$), lower susceptibility at the remanence and larger total susceptibility than that measured by applying the field along the *Y* axis ($m_r = 0.4$). The reduced remanence obtained from both the experiments and the simulations corresponds to the possibility of implementing, by means of the considered array, elevated stray field magnitudes in the vicinity of the array motifs (the field could reach about 17 000 G at the lateral surfaces of the motifs) like those required for the implementation of magnetostatic-based applications [7, 8]. The results for micromagnetic simulations of the hysteresis loops measured in array A2 are also shown (continuous line) in figures 4(a) and (b) for fields applied along the *X* and *Y* axes, respectively. From a comparison of those simulational results with experiment it is possible to observe: (i) that the simulations reproduce, for both field directions, a global magnetization reversal mediated

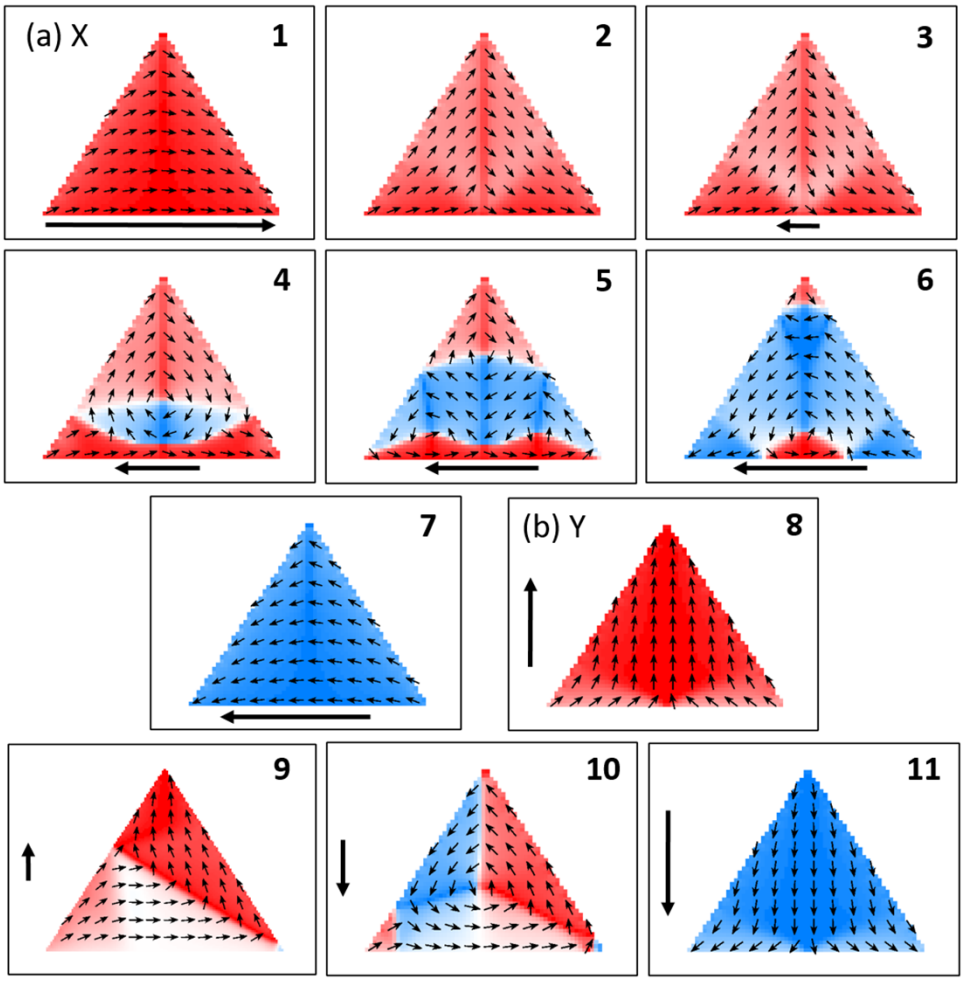


**Figure 3.** Array A1: magnetic moment configurations obtained from the micromagnetic simulations of the motif reversal process with the applied field oriented along (a) the *X* axis and (b) the *Y* axis. The arrows in each configuration indicate the applied field direction, sign and approximate magnitude. The field sequence runs from saturating positive fields to saturating negative ones. The labels correspond to the (H, M) points indicated in figure 2.

by two large irreversibilities and a loop constriction at close to zero magnetization, and (ii) that coincidently with the experiment, a lower remanence is obtained for the loop simulated by applying the field along the *Y* axis than for that calculated with the field parallel to the *X* axis. The configurations obtained for the moment structures at the remanences (label 2 in figure 5(a) for an *X* axis field, and label 7 in figure 5(b) for a *Y* axis field) correspond to the buckle type (centered at a point below the motif base) and to a slightly distorted buckle type (centered at a point located outside the NT and close to one of its shorter sides), respectively.

The high remanence measured along the *X* axis is a direct consequence of the large difference in effective anisotropy energy between the moments directed along *X* and *Y* directions. Whereas the *X* direction corresponds to the easiest direction of the configurational and MAE contributions, the *Y* axis is an easy MAE direction but the hardest configurational one. The lack of compensation between the hardest configurational axis and the associated MAE one results in the need to expend a large amount of energy to take the moments from the *X* axis towards the *Y* direction and form the vortex. Concomitantly, the inter-NT interactions would also reduce the energy of the moments oriented along the *X* axis, due to the occurrence at short distances along that direction of poles of opposite sign in neighboring motifs [7]. However, for fields directed along the *Y* axis the inter-NT interactions do not stabilize the remanence as much as along the *X* axis since the larger inter-NT distance (and the higher multipolar moment of the close-to-vertex pole densities) does not result in important magnetizing fields inside the first neighbor motif along the *Y* axis [7].

In array A2 the moment configuration corresponding to the departure from positive saturation and resulting from the irreversibility of the lower demagnetizing field is, for both applied field directions, a vortex-like structure (adapted to the morphology at the lateral surfaces of the NTs, where the moments are directed significantly away from the surface normal directions in order to both minimize the pole density and spread the poles in as large a volume as possible). The vortex core is nucleated inside the motifs in the $H_n$ field, (labels 3 and 8 in figure 5, corresponding to (*M*,*H*) points labeled 3 and 8 in figures 4(a) and (b), respectively). In the case of a field applied parallel to the *X* axis, our simulations show that the vortex enters the NTB at the midpoint of its base, whereas when the field is parallel to the *Y* axis the point at which the

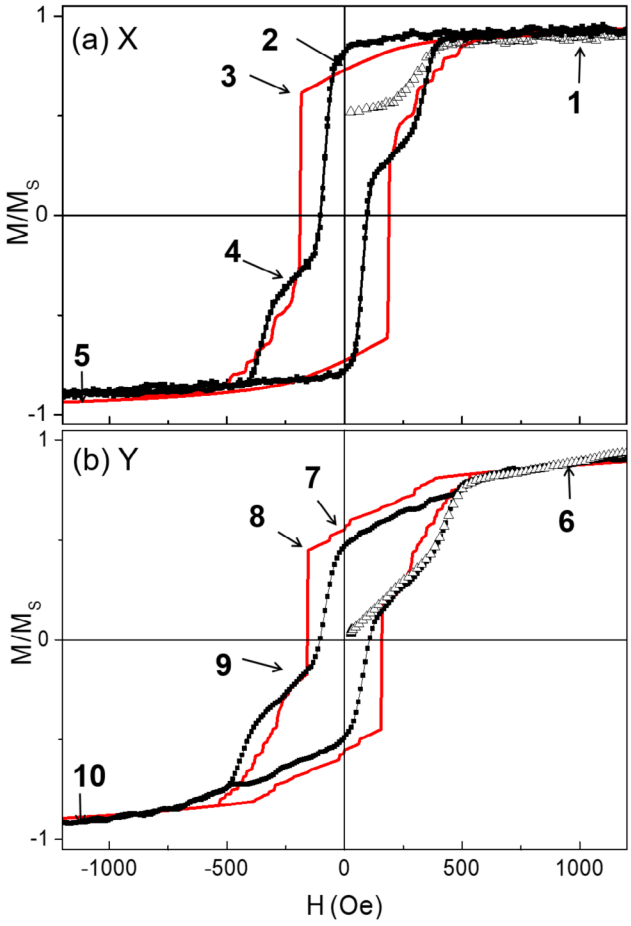


**Figure 4.** Array A2: experimental (symbols joined by lines) and calculated (continuous lines) hysteresis loops corresponding to applied fields directed along the *X* axis (a) and *Y* axis (b). The labels on these figures correspond to those tagging the moment configurations obtained from the micromagnetic simulations shown in figure 5. The magnetization curves measured by applying the field along (a) the *X* axis and (b) the *Y* axis, with the array in a remanent state prepared after saturation with the field applied along *Y* and *X* axes, respectively, are plotted with open triangular symbols.

vortex is nucleated corresponds to the midpoint of one of the lateral sides of the NTB. The second irreversibility, occurring at larger demagnetizing fields and approaching negative saturation of the array, corresponds to displacement of the vortex core out of the motifs (vortex annihilation). In the field range between $H_n$ and $H_{an}$, and for increasing demagnetizing fields, the vortex moves from the nucleation site towards the center of the NTB; it stabilizes close to that point due to the effective surface pole and MSE minimization resulting from the centered solenoidal moment structure (labels 4 and 9 in figure 5, corresponding to ($M$, $H$) points labeled 4 and 9 in figures 4(a) and (b), respectively), and it drifts away from that central position towards the annihilation point to finally leave the motif when the demagnetizing field increases to $H_{an}$. As can be seen in figure 5, the vortex leaves the motif through the vertex opposite the nucleation site, irrespective of the orientation of the applied field.

For a quantitative comparison of the experimental and simulated $H_n$ and $H_{an}$ values, our modeling results yield higher values and more collective behavior for the nucleation field than the experimentally measured ones. This is a consequence of the absence in the model of any nucleation-favoring defects (either morphological or related to the local magnetic properties). However, the simulated vortex annihilation processes more closely coincide with the experimental data, presumably due to the nature of the moment configuration transition from an off-center solenoidal one to a quasi-uniform orientation of the moments (globally involving smaller variations of moment orientation than the nucleation process).

The moment configuration at remanence deserves attention. Micromagnetic simulations on Permalloy have shown the possibility of the occurrence of both the 'Y' and the 'buckle' configurations. Namely, the 'Y' configuration has been reported to be only realizable in triangular Permalloy dots under restrictive conditions (i.e. sharp corners and equilateral NTB sides having lengths below 200 nm) [30, 33]. For array A2, a question arises about the possible occurrence of the 'Y' remanence configuration when the field is applied parallel to the *Y* axis due to the fact that the magnetocrystalline anisotropy has an easy axis along that direction.

However, the configuration obtained from the micromagnetic simulations (label 7 in figure 5(a)) is clearly of the 'buckle' type and it is associated with an *X* component of the motif magnetization that is different from zero. In order to experimentally elucidate the moment configuration at remanence that actually occurs in A2, we have implemented an applied field variation sequence allowing us to evaluate the saturation remanence as follows: (i) the array is first saturated by applying a field along the *Y* axis, after that the field is reduced to zero which takes the sample to the corresponding remanent state; (ii) the array is then rotated so as to align the applied field direction with the *X* axis and a magnetization curve up to saturation is measured. That curve is shown in figure 4(a) (open triangular dots). The measured reduced remanence corresponds to a value of about 0.5 in good agreement with the value of 0.48 obtained from the micromagnetic simulations [7]. The remanence configuration corresponds, essentially, to orientation along the *X* axis for the moments in most of the lower half of the NTB and orientation along the *Y* axis for the moments on the upper half of the NTB (label 7 in figure 5(b)). A different result is expected when A2 is first saturated along the positive *X* axis and is then kept in its remanent configuration. The simulations (label 2 in figure 5(a)) indicate that the moments near the base are almost parallel to the *X* axis, whereas those in the upper regions of the NTB point essentially up and down in the left and right regions of the motifs, respectively. As a consequence, the remanent magnetization of the NTs should in this case have a null *Y* component. A field sequence similar to that previously considered was applied to disclose the remanent moment configuration of the NTs after positive saturation along the *X* axis. The array was rotated so as to align the *Y* axis with the field direction and a magnetization curve up to saturation was measured. That magnetization curve is plotted using open triangular symbols in figure 4(b) and, as can be seen, its starting point corresponds to close-to-zero magnetization, in agreement with the configuration obtained from the simulations.

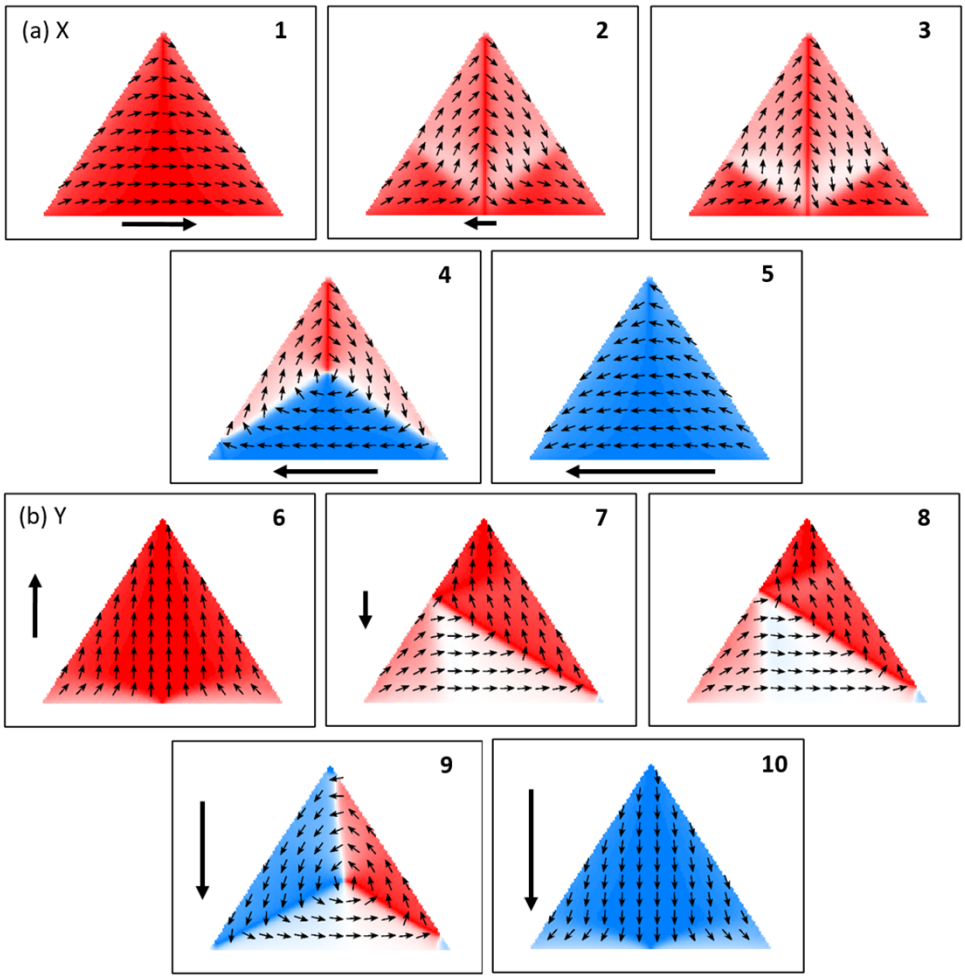


**Figure 5.** Array A2: magnetic moment configurations obtained from micromagnetic simulations of the motif reversal process with the applied field oriented along (a) the *X* axis and (b) the *Y* axis. The arrows in each configuration indicate the direction, sign and approximate magnitude of the applied field. The field sequence runs from saturating positive fields to saturating negative ones. The labels correspond to the (*H*,*M*) points indicated in figure 4.

To gain further insight into the vortex nucleation and annihilation processes, 'half loops' [24] were measured in array A2 (figure 6) by (i) starting at (positive) saturation, (ii) applying a demagnetizing field larger than the nucleation field but smaller than the annihilation one and then (iii) decreasing the demagnetizing field to zero and then increasing the magnetizing one in order to take the sample back to positive saturation. By implementing this field variation sequence our purpose was to compare the vortex annihilation processes observable when they take place in different environments, such as those associated with the positive (half loop) and the negative (full loop) saturations. As can be seen in figure 6, for fields applied along the *X* axis the annihilation event associated with the half loop takes place at approximately 280 Oe, whereas that corresponding to the full loop occurs at about 370 Oe. According to our simulations, a vortex is nucleated at $H_n$ at the midpoint of the NTB base and then moves to the motif center upon application of slightly larger negative fields. Once the demagnetizing field is reversed and increased to achieve positive saturation, the vortex is annihilated at a field (half-loop annihilation) that is experimentally different from that associated with the annihilation process that would occur close to negative saturation (full loop annihilation). The difference between the fields required to annihilate the vortex in these different environments clearly suggests that the points at which the vortex leaves the motif are different in the half and the full loops. More concretely, the smaller annihilation field associated with the half loop indicates that, for that field

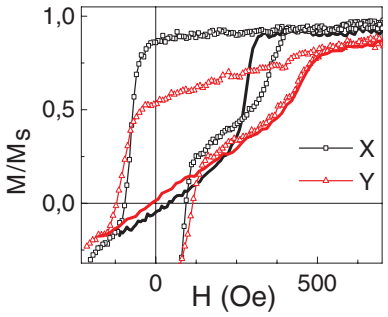


**Figure 6.** Array A2: comparison of the annihilation processes observable along the *X* and *Y* axes after submitting the array to full applied field loops (see text; data shown using open symbols) and to half applied field loops (see text; data shown using continuous lines).

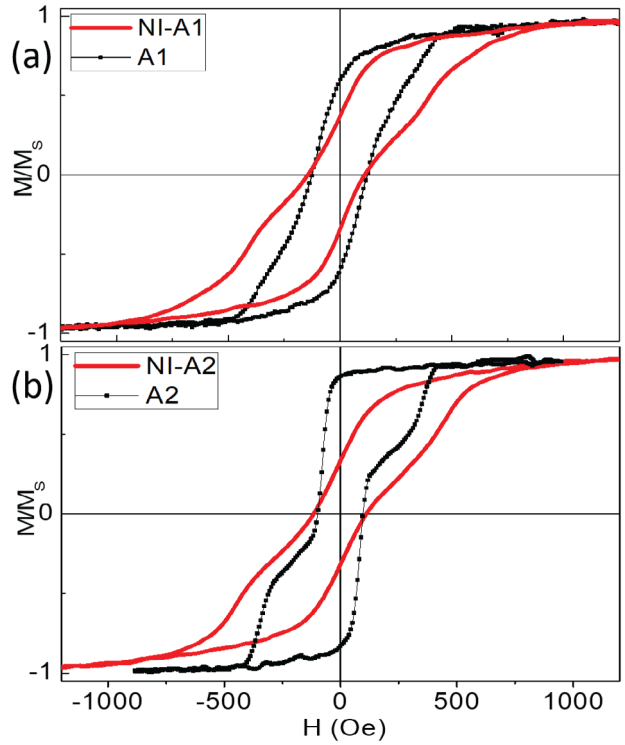


**Figure 7.** (a) Comparison of the hysteresis loops (field applied along the *X* axis) measured in array A1 (solid symbols joined by lines) and array NI-A1 (continuous line). (b) Comparison of the hysteresis loops (field applied along the *X* axis) measured in array A2 (solid symbols joined by lines) and array NI-A2 (continuous line).

variation routine, the vortex does not annihilate at the upper vertex of the NTB (as our simulation results showed for the full loop case), but at a place where the local demagnetizing fields are lower than those occurring at the vertices, as, for example, the nucleation region or the center of the sides. A different annihilation behavior is observed when the field is applied along the *Y* axis (see figure 6), since in this case no differences were observed between the half and full loop experimental annihilation field values (and the vortex displacement path should coincide with that already described for the full loops, that is, the vortex is nucleated at one of the NTB sides, moves to the motif center and annihilates at the vertex opposite the nucleation site). This shows that the implementation of morphological asymmetries or the application of fields along different directions from the morphological symmetry axes allow the selection of the nucleation and annihilation sites, as has been reported in polycrystalline Ni NTs with similar sizes [23] and in asymmetric polycrystalline Co dots [17, 24].

In order to identify the role in the array reversal process of the dipolar interactions between motifs, figure 7 compares the *X* axis hysteresis loop measured in array A1 (A2) with the equivalent loop measured in array NI-A1 (NI-A2), the latter arrays integrating NTs that have a similar size to those in A1 (A2) but inter-NT separation of over twice that of the former arrays. As can be seen in figure 7, the loops measured in the weakly interacting NT arrays are sheared so as to exhibit larger saturation fields and a broader distribution of nucleation fields. In the case of the almost non-interacting motifs, the reversal is essentially local without any collective element. The loop shear results from the distribution of local properties (morphological and magnetic) that influence the nucleation and annihilation processes. Interestingly, the global coercivity of both types of array approximately coincides. This result is due to the fact that in both array types vortices mediate the reversal process and that centered vortices are linked to close-to-zero motif magnetization and, therefore, to minimum inter-motif interactions. Also, the presence in arrays NI-A1 and NI-A2 of vortices exclusively originating from the motif shape and effective anisotropy energy, and which have the ability to gain a stable position near to the motif center, is the origin of a very low remanence compared with that measured in the interactive NT array A1 (A2), where interactions contribute to a more collective behavior. Considering now the experimental data on the nucleation field, figures 7(a) and (b) show that the nucleation process is shifted in arrays A1 and A2 to larger negative fields than those associated with that process in the corresponding weakly interactive arrays NI-A1 and NI-A2. The nucleation field of array A1 (A2) occurs in the second quadrant, between 27 and 90 Oe (70 Oe and 130 Oe), whereas the nucleation fields of the weakly interactive arrays are close to zero or even positive. This shift is understood as a consequence of the larger collectiveness of the demagnetization of these arrays which is mediated by the inter-motif dipolar interactions. It is important to remark here that it is expected that interactions in the close-to-saturation field regions (as those corresponding to the remanence and nucleation) could play a more significant role than in the field range corresponding to close-to-zero magnetization, where vortices very effectively minimize the poles at the motif surfaces. Finally, the global annihilation field in A1 (A2), $H_{an} \approx 390$ Oe (350 Oe), is lower than that measured in array NI-A1 (NI-A2), $H_{an} \approx 430$ Oe (475 Oe), which indicates that the inter-NT magnetostatic interactions, similarly to the case of interacting magnetic nanoparticles and in agreement with previously reported results obtained on nanodots [34], make possible the occurrence of demagnetizing processes involving several NTs. Despite this, no indications of collectiveness were found in our simulated system; this could be related to the highly anisotropic nature of the interaction (more intense along the *X* axis than along the *Y* axis due to the motifs and array dimensions [35]), and to the fact that the reduced number of simulated motifs did not even allow implementation of a complete set of nearest motif neighbors.

To analyze in further detail the combined effects of the configurational anisotropy, the MAE and the dipolar interactions between neighboring NTs we have measured the angular evolution of the hysteresis parameters. Figure 8 shows (solid symbols) the angular dependence of the reduced remanence, $m_r$, obtained from the hysteresis loops measured in arrays A1 and A2. The reduced remanences exhibit a two-lobed-type angular dependence (effective uniaxial symmetry), with a minimum occurring in the *Y* axis direction ($\theta = \pi/2$) from which it monotonically increases up to the almost equivalent maxima observable in both arrays at the two *X* axis senses ($\theta = 0$ and $\pi$). The minimum at $\theta = \pi/2$ is clearly linked to the occurrence of a maximum in the array's total energy along

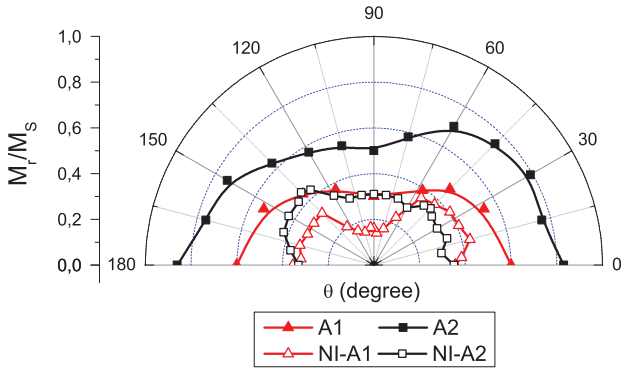


**Figure 8.** Angular dependence of the reduced saturation remanence measured along the *X* axis in array A1 (solid red triangles), array A2 (solid black squares), array NI-A1 (open red triangles) and array NI-A2 (open black squares).

that direction (the *Y* axis). The origin of the uniaxial behavior should be related to: (i) the reduced symmetry of the motifs, which incorporate isosceles NTBs with bases slightly longer than their other sides, and for which the alignment of the motif magnetization along the base direction has lower energy than that corresponding to a magnetization alignment parallel to the other motif edges; (ii) in the A2 array case, the coincidence of a MAE easy axis with the easiest configurational one; and (iii) the inter-motif interactions which, due to the shorter inter-NT distance along the *X* axis (see figure 1), favor moment orientation along that axis (since, in array A1, a MAE hard axis partly compensates the easiest configurational one, the remanences in A1 are lower than in A2 even though uniaxial symmetry is preserved in the former array due to the isosceles shape of the NT bases and the occurrence of inter-motif interactions favoring the *X* direction). The data on the angular dependence of the reduced remanence corresponding to arrays NI-A1 and NI-A2 are plotted in figure 8 using open symbols. As can be seen, the remanence of arrays A1 and A2 varies in a range between 0.3 $M_s$ and 0.85 $M_s$, whereas that of arrays NI-A1 and NI-A2 is clearly lower, varying between 0.15 $M_S$ and 0.45 $M_S$ in plausible correspondence with the occurrence of weaker interactions in the latter arrays. However, the uniaxial symmetry with a hard axis along $\theta = \pi/2$ is observable in the four cases, which strongly suggests that the origin of the effective anisotropy symmetry corresponds to the coincidence of an easy configurational axis with a MAE one with a smaller influence of the inter-NT interactions [35].

The annihilation processes involve a transition from an extended, non-homogeneous magnetic moment configuration to a close-to-saturated one, which implies a large increase in MSE energy due to the appearance (upon annihilation) of the poles at the regions close to the base and lateral sides of the NTBs. As can be seen in figures 9(a) and (b), the annihilation fields of the weakly interactive arrays NI-A1 and NI-A2 are, for most directions, larger than those of the corresponding interactive arrays A1 and A2. The symmetry of the angular dependences of the annihilation fields measured in the NI-A1 (NI-A2) arrays is no longer uniaxial but quasi-triaxial and results from the convolution of the biaxial in-plane symmetry linked to the MAE and the triaxial symmetry [29, 30]

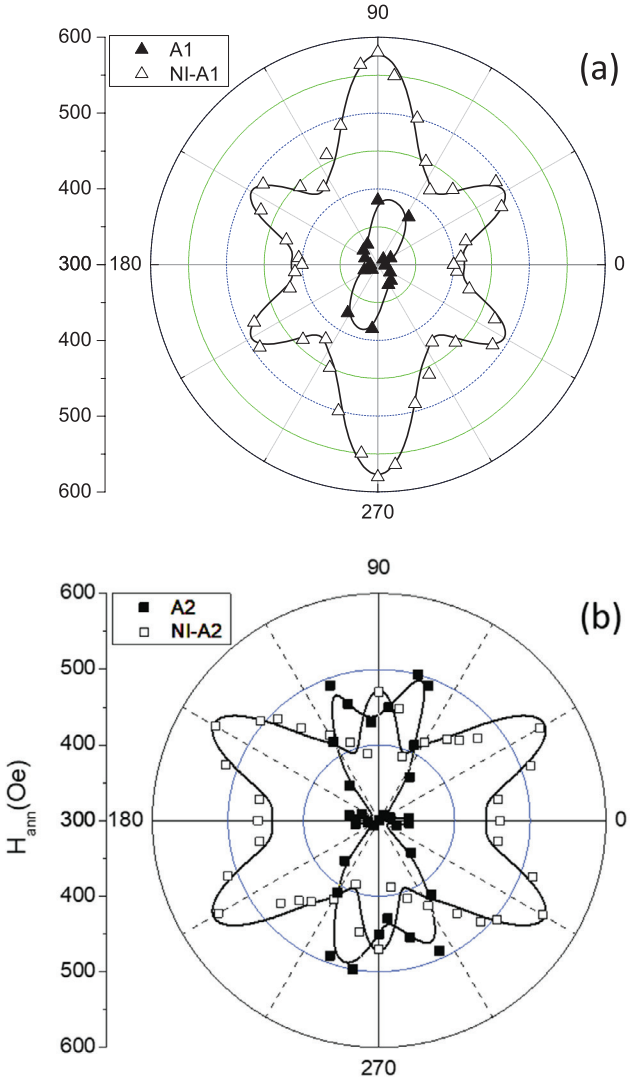


**Figure 9.** Angular dependence of the annihilation field for (a) arrays with the ' × ' configuration of crystal easy axes (array A1 (solid triangles) and array NI-A1 (open triangles)) and (b) arrays with the '+' configuration of crystal easy axes (array A2 (solid squares) and array NI-A2 (open squares)).

associated with the configurational anisotropy, with the latter predominating over the former [29]. This last point is clear from the annihilation field obtained in array NI-A1 along the *Y* axis, which is larger than that measured along that same direction in array NI-A2. In array NI-A1, two configurational and MAE hard axes coincide along the *Y* axis, whereas in array NI-A2 a configurational hard axis is partly compensated by an easy MAE direction [35].

The angular evolutions of the annihilation fields of arrays A1 and A2 exhibit lower symmetries than those found in the weakly interactive arrays. Array A1 presents an absolute minimum of the annihilation field when the field is applied along the *X* direction (coincident with the easiest configurational anisotropy direction and a hard MAE one) and a maximum annihilation field when the demagnetizing field is applied along *Y* (a direction coincident with hard MAE and configurational anisotropy directions). The annihilation field of array A2 increases when the field orientation is changed

from directions parallel to the base of the NTBs (*X* axis) to directions close to the *Y* axis, although with a more complex evolution than that found in A1, i.e. a relative minimum of the annihilation field appearing along the *Y* direction. That minimum could be related to the lower magnitude (compared with the *X* axis reversal process) of the inter-motif interactions associated with the alternating negative and positive poles present in neighboring motifs along the *Y* axis (highly inhomogeneous) in demagnetizing fields.

## Conclusions

We have shown how the occurrence of MAE in single-crystal Fe nanomagnets is linked to the possibility of getting sizable remanence to saturation ratios of up to 0.85 and stray fields in the immediate vicinity of the nanoelements fully appropriate for the implementation of magnetostatic field-based applications. This result allows us to identify array A2 as the most appropriate for the implementation of superconducting vortex ac movement rectifiers.

The elevated remanences we obtain result from the convolution (in order of prevalence) of a configurational easy axis (with symmetry reduced from that corresponding to the regular triangular morphology), a MAE easy axis ('+' configuration) and of close-to-saturation magnetizing interactions resulting from the short inter-motif distances along the direction corresponding to the configurational and MAE easy axes. The remanent moment configuration corresponds to a buckle configuration stabilized by the large difference in energy between the easy *X* axis and the hard *Y* one. The demagnetization proceeds, at motif scale, through the following sequence: vortex nucleation, displacement, stabilization and annihilation. There exists, however, a collective contribution to the demagnetization, apparent from the obtained hysteretic parameter values and the different annihilation fields measured with the vortices evolving under different field histories.

Globally, the effective symmetry associated with the acquisition of remanence corresponds, in both interacting and weakly interacting arrays, to the uniaxial type, unlike in previous results reported for Ni polycrystalline NT arrays [19, 23]. As for the nucleation fields of the vortices (which largely govern the stability of the remanence), they are small or even zero in the case of weakly interacting arrays where the departure from saturation is governed by local motif properties, but increase, in the interacting arrays, up to values in the tens of Oe range (useful for applications) due to the inter-motif interactions occurring in the field region close to saturation.

Finally, the angular dependence of the annihilation fields is evident in the contributions of the configurational anisotropy and the MAE. The interactions are again apparent from the angular dependence of the annihilation field measured in the A1 and A2 arrays for which an approximately uniaxial symmetry and a quasi-biaxial one are observed, respectively. The differences between the behaviors of these two arrays are understood to be related to the large differences between the pole distributions present in the *X* and *Y* axis pre-annihilation states and the stray fields that originate from these.

## Acknowledgments

F C, F J P, M S A, U U and J M G would like to acknowledge the Spanish Ministry of Economy and Competitiveness Grant Nos. MAT2013-47878-C2-1-R, MAT2013-47878-C2-2-R and MAT2016-80394-R. A G, E M G and J L V are grateful for support from Spanish Ministry of Economy and Competitiveness Grant No. FIS2016-76058-C4-1-R (AEI/FEDER,EU) and Comunidad de Madrid Grant No. P2013/MIT-2850. IMDEA Nanociencia acknowledges support from the 'Severo Ochoa' Program for Centers of Excellence in R&D (MINECO, Grant SEV-2016-0686).

## ORCID iDs

J L Vicent https://orcid.org/0000-0001-9343-7671
J M Gonzalez https://orcid.org/0000-0001-7944-340X

## References

[1] Haldar A, Kumar D and Adeyeye A O 2016 *Nat. Nanotechnol.* **11** 437
[2] Martin J I, Nogues J, Liu K, Vicent J L and Schuller I K 2003 *J. Magn. Magn. Mater.* **256** 49
[3] Haldar A and Adeyeye A O 2015 *ACS Nano* **10** 1690
[4] Nikonov D E and Young I A 2013 *Proc. IEEE* **101** 2498
[5] Bader S D 2006 *Rev. Mod. Phys.* **78** 1
[6] Paz E, Cebollada F, Palomares F J, García-Sánchez F and González J M 2010 *Nanotechnology* **21** 255301
[7] Gómez A, González E M, Iglesias M, Sánchez N, Palomares F J, Cebollada F, González J M and Vicent J L 2013 *J. Phys. D: Appl. Phys.* **46** 095302
[8] Nanayakkara K, Vasil'evskii I S, Eremin I S, Kolentsova O S, Kargin N I, Anferov A and Kozhanov A 2016 *J. Appl. Phys.* **119** 233906
[9] Kozhanov A, Allen S and Palmstrom C 2012 *US Patent* 8198919
[10] Cowburn R P 2000 *J. Phys. D: Appl. Phys.* **33** R1
[11] Cowburn R P, Adeye A O and Welland H E 1998 *Phys. Rev. Lett.* **81** 5414
[12] Cowburn R P, Koltsov D K, Adeye A O, Welland H E and Tricker D M 1999 *Phys. Rev. Lett.* **83** 1042
[13] Barman A, Barman S, Kimura T, Fukuma Y and Otani Y 2000 *J. Phys. D: Appl. Phys.* **43** 422001
[14] Shinjo T, Okuno T, Hassdorf R, Shigeto K and Ono T 2000 *Science* **289** 930
[15] Prejbeanu I L, Natali M, Buda L D, Ebels U, Lebib A, Chen Y and Ounadjela K 2002 *J. Appl. Phys.* **91** 7344
[16] Roshchin I V *et al* 2009 *Europhys. Lett.* **86** 67008
[17] Dumas R K, Gredig T, Li C P, Schuller I K and Liu K 2009 *Phys. Rev.* B **80** 014416
[18] Guslienko K Y and Metlov K L 2001 *Phys. Rev.* B **63** 100403
[19] Jaafar M, Yanes R, Asenjo A, Chubykalo-Fesenko O, Vázquez M, González E M and Vicent J L 2008 *Nanotechnology* **19** 285717

[20] Vargas N M, Allende S, Leighton B, Escrig J, Mejiía-López J, Altbir D and Schuller I K 2011 *J. Appl. Phys.* **109** 073907
[21] Wu K M, Horng L, Wang J F, Wu J C, Wu Y H and Lee C M 2008 *Appl. Phys. Lett.* **92** 262507
[22] Vavassori P, Zaluzec N, Metlushko V, Novosad V, Ilic B and Grimsditch M 2004 *Phys. Rev.* B **69** 214404
[23] Jaafar M, Yanes R, Perez de Lara D, Chubykalo-Fesenko O, Asenjo A, Gonzalez E M, Anguita J V, Vazquez M and Vicent J L 2010 *Phys. Rev.* B **81** 054439
[24] Dumas R K, Gilbert D A, Eibagi N and Liu K 2011 *Phys. Rev.* B **83** 060415
[25] Mejía-López J, Altbir D, Romero A H, Battle X, Roshchin I V, Li C-P and Schuller I K 2006 *J. Appl. Phys.* **100** 104319
[26] Novosad V, Grimsditch M, Guslienko K Y, Vavassori P, Otani Y and Bader S D 2002 *Phys. Rev.* B **66** 052407
[27] Grimsditch M, Jaccard Y and Schuller I K 1998 *Phys. Rev.* B **58** 11539
[28] Paz E, Cebollada F, Palomares F J, Gonzalez J M, Martins J S, Santos N M and Sobolev N A 2012 *J. Appl. Phys.* **111** 123917
[29] Gomez A, Cebollada F, Palomares F J, Sanchez N, Gonzalez E M, Gonzalez J M and Vicent J L 2014 *Appl. Phys. Lett.* **104** 102406
[30] Thevenard L, Zeng H T, Petit D and Cowburn R P 2009 *J. Appl. Phys.* **106** 063902
[31] Donahue M J and Porter D G 1999 OOMMF User's Guide version 1.0 *Interagency Report* NISTIR 6376 (Gaithersburg, MD: National Institute of Standards and Technology)
[32] Chikazumi S 1978 *Physics of Magnetism* (Malabar, FL: Krieger Publishing Co.) p 186
[33] Koltsov D K, Cowburn R P and Welland M E 2000 *J. Appl. Phys.* **88** 5315
[34] Vavassori P, Bisero D, Bonanni V, Busato A, Grimsditch M, Lebecki K M, Metlushko V and Ilic B 2008 *Phys. Rev.* B **78** 174403
[35] Sanchez-Agudo M, Cebollada F and Gonzalez J M 2018 *Physica* B **549** 35–9